

High Sulfur Loading and Capacity Retention in Bilayer Garnet Sulfurized-Polyacrylonitrile/Lithium-Metal Batteries with Gel Polymer Electrolytes

Changmin Shi, Saya Takeuchi, George V. Alexander, Tanner Hamann, Jonathan O'Neill, Joseph A. Dura, and Eric D. Wachsman*

The cubic-garnet ($\text{Li}_7\text{La}_3\text{Zr}_2\text{O}_{12}$, LLZO) lithium–sulfur battery shows great promise in the pursuit of achieving high energy densities. The sulfur used in the cathodes is abundant, inexpensive, and possesses high specific capacity. In addition, LLZO displays excellent chemical stability with Li metal; however, the instabilities in the sulfur cathode/LLZO interface can lead to performance degradation that limits the development of these batteries. Therefore, it is critical to resolve these interfacial challenges to achieve stable cycling. Here, an innovative gel polymer buffer layer to stabilize the sulfur cathode/LLZO interface is created. Employing a thin bilayer LLZO (dense/porous) architecture as a solid electrolyte and significantly high sulfur loading of 5.2 mg cm^{-2} , stable cycling is achieved with a high initial discharge capacity of 1542 mAh g^{-1} (discharge current density of 0.87 mA cm^{-2}) and an average discharge capacity of 1218 mAh g^{-1} (discharge current density of 1.74 mA cm^{-2}) with 80% capacity retention over 265 cycles, at room temperature ($22 \text{ }^\circ\text{C}$) and without applied pressure. Achieving such stability with high sulfur loading is a major step in the development of potentially commercial garnet lithium–sulfur batteries.

1. Introduction

Inorganic solid-state Lithium-Sulfur (Li–S) batteries are a promising next-generation energy storage system due to the low cost and high theoretical energy density of sulfur (2600 Wh kg^{-1} and 2800 Wh L^{-1}) and the nonflammability of ceramic solid-state electrolytes (SSEs).^[1–6] Among all types of SSEs in Li–S batteries, the sulfide electrolyte and cubic phase Li-filled garnet ($\text{Li}_7\text{La}_3\text{Zr}_2\text{O}_{12}$, LLZO) electrolytes are the most promising candidates because of their high ionic conductivity at room temperature.^[7–11] Unlike the sulfide-based SSE, LLZO is more chemically stable against Li metal and does not produce toxic gases when exposed to air and moisture, making it a potentially preferable SSE for solid-state Li–S batteries.^[12–15]

Nevertheless, these exist critical stability limitations on both the anodic and the cathodic sides of the garnet electrolyte. On the Li metal anode side, published results demonstrate Li dendrite growth in LLZO,^[12,16] especially between the grain boundaries.^[12] To overcome this issue, multiple strategies have been explored, such as building a lithophilic layer at the LLZO/Li-metal interface^[17] and applying a polymer interlayer to improve the physical contact between LLZO/Li-metal.^[18] In addition to the chemical modifications at the interface, we thoroughly resolved the Li dendrite issue by implementing unique porous/dense/porous LLZO “trilayer” and porous/dense LLZO “bilayer” architectures^[19–21] to inhibit dendrite growth and enable high areal current densities of 10 mA cm^{-2} in Li–Li symmetric cells without applied pressure.^[19] The porous layer can accommodate the volume change of the Li metal side during cell cycling^[22] and can also withstand high Li penetration stress and high current density.^[23] On the sulfur cathode side, studies have indicated that the sulfur cathode/Ta-doped LLZO (Ta-LLZO) interface can be unstable, with the sulfur reacting with La-segregation phases at the Ta-LLZO surface^[24] and significant ($\approx 80\%$) volume expansion during discharge^[25,26] that applies significant stress/strain to the sulfur cathode/Ta-LLZO interface, potentially resulting in crack formation in the solid ceramic phase.

C. Shi, S. Takeuchi, G. V. Alexander, T. Hamann, J. O'Neill, E. D. Wachsman
Department of Materials Science and Engineering
The University of Maryland
College Park, MD 20742, USA
E-mail: ewach@umd.edu

C. Shi, S. Takeuchi, G. V. Alexander, T. Hamann, J. O'Neill, E. D. Wachsman
Maryland Energy Innovation Institute
The University of Maryland
College Park, MD 20742, USA
S. Takeuchi, J. A. Dura
Center for Neutron Research
National Institute of Standards and Technology
Gaithersburg, MD 20899, USA

 The ORCID identification number(s) for the author(s) of this article can be found under <https://doi.org/10.1002/aenm.202301656>

© 2023 The Authors. Advanced Energy Materials published by Wiley-VCH GmbH. This is an open access article under the terms of the Creative Commons Attribution License, which permits use, distribution and reproduction in any medium, provided the original work is properly cited.

DOI: 10.1002/aenm.202301656

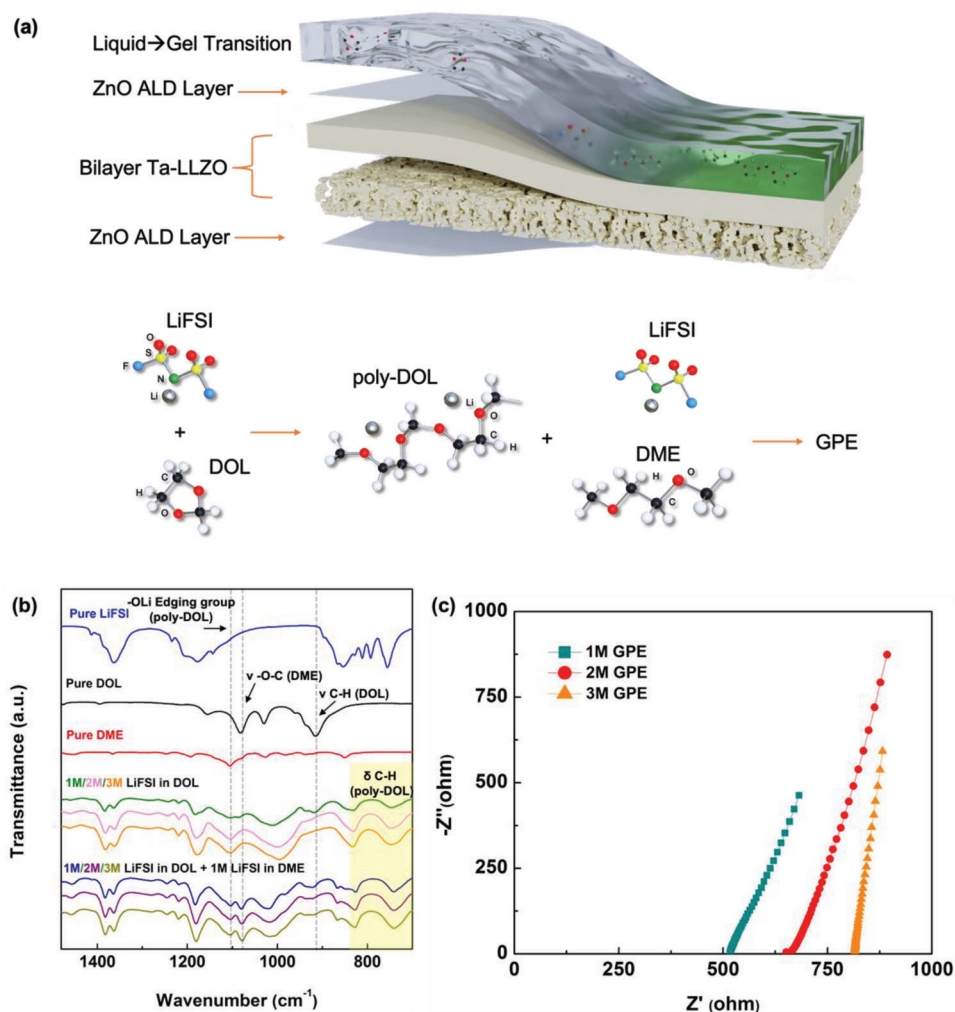


Figure 1. a) Schematic illustration of our cell configuration and b) the in situ formed GPE on the bilayer LLZO. c) The ATR-FTIR of the pure LiFSI, 1,3 Dioxolane (DOL), polymerized DOL (poly-DOL), 1,2-Dimethoxyethane (DME), and the GPE. (c). EIS measurement of different LiFSI concentrations in GPE. The frequency range is from 0.1 MHz to 100 Hz at an amplitude of 25 mV.

In our previous work, we added a Polyethylene Oxide (PEO)-based interlayer between the sulfur cathode and bilayer Ta-LLZO to improve the chemical and mechanical stability of the interface during cycling, with the resulting Li-S battery demonstrating a high initial discharge capacity of 1307 mAh g⁻¹.^[24] However, this solution required a relatively large amount of catholyte (20 μL cm⁻²), reducing cell energy density. Likewise, the low sulfur mass loading and the high mass of thick LLZO separators^[27–30] in these cells negatively impacted their energy densities.

To address these issues, we have developed an innovative gel polymer electrolyte (GPE) as a catholyte to replace the PEO as a stabilizing interlayer between the cathode and the thin Ta-LLZO bilayer electrolyte (Figure S1, Supporting Information). The GPE was synthesized in situ on the dense Ta-LLZO surface, to stabilize the sulfur cathode/Ta-LLZO interface while maintaining good physical contact. In addition, instead of using elemental sulfur as cathode active material (CAM) as we demonstrated before,^[24] sulfurized polyacrylonitrile (SPAN) was chosen as the sulfur ac-

tive material due to its demonstrated excellent cycling stability, higher electronic conductivity, and less volume change than elemental sulfur.^[31–33]

2. Results and Discussion

2.1. In Situ Gel Polymer Electrolyte

Figure 1a shows a schematic of our innovative GPE/Ta-LLZO hybrid electrolyte. A thin ZnO layer was deposited on both sides of the bilayer Ta-LLZO to improve wetting between the Li metal and the Ta-LLZO (on the anode side)^[19,21] with an average thickness of ≈9 nm (Figure S2, Supporting Information). By using ALD technique, the inner surface of the porous layer can be uniformly coated.^[34] This improved wetting ability was due to the reaction between ZnO and Li metal to form Li-Zn alloy, through which the Li diffuses along the ZnO ALD layer and wets the Ta-LLZO surface.^[34] During cell fabrication, we observed that the ZnO ALD coating layer also improved the wetting between the

GPE and the Ta-LLZO (on the cathode side). This is due to the inherent hydrophilic nature of the ZnO^[35] and also likely due to increased surface free energy^[36] of Ta-LLTZO after coating with the thin ZnO ALD layer. The GPE interlayers were synthesized with three different Lithium bis(fluorosulfonyl)imide (LiFSI) salt molar concentrations of 1 M ($M \equiv \text{mol L}^{-1}$), 2 M and 3 M. For the sake of brevity, the mixtures will be referred to as “1 M GPE”, “2 M GPE”, and “3 M GPE”, respectively.

The GPE was characterized by Attenuated Total Reflection-Fourier transform infrared spectroscopy (ATR-FTIR) in Figure 1b. Within the fingerprint region (i.e., below 1500 cm^{-1}), the 1 M GPE showed -C-H- out-of-plane stretching of the 1,3 Dioxolane (DOL, i.e., the GPE precursor) transmittance peak at 916 cm^{-1} , indicating the presence of residual unpolymerized precursor. In contrast, no residual unpolymerized precursor was observed in the ATR-FTIR spectra for the 2 M GPE and 3 M GPE, indicating they were completely polymerized. The detail regarding the GPE peaks is provided in Table S1 (Supporting Information).

The average GPE thickness is 2.5–3 μm . The conductivity of the GPEs was measured using electrochemical impedance spectroscopy (EIS). From the Nyquist plot in Figure 1c, the average ionic conductivity of 1, 2, and 3 M GPE at 22 °C was 5.6, 4.5, and 3.5 mS cm^{-1} (Figure S3, Supporting Information), respectively. Because of their high conductivity, the average area specific resistance (ASR) of the bulk 1, 2, and 3 M GPEs contributes only 4.7, 5.6, and 8.6 $\text{ohm}\cdot\text{cm}^2$, to the total cell ASR. The ionic conductivity of the GPEs were not tested at elevated temperature due to their thermal instability above room temperature (Figure S4, Supporting Information).

The impedance of the GPE/Ta-LLZO interface (for 1, 2, and 3 M) and the GPE/SPAN cathode interface was also measured (Figure S5, Supporting Information). The equivalent circuits of these systems are shown in Figure S5a,b (Supporting Information). The overall interfacial ASR between the GPE and the Ta-LLZO was 31 $\text{ohm}\cdot\text{cm}^2$ (1 M) (Figure S5c, Supporting Information), 46 $\text{ohm}\cdot\text{cm}^2$ (2 M) (Figure S5d, Supporting Information), and 63 $\text{ohm}\cdot\text{cm}^2$ (3 M) (Figure S5e, Supporting Information), respectively. The overall interfacial ASR between the GPE and the SPAN cathode was very low, measuring only 3.5 $\text{ohm}\cdot\text{cm}^2$ (1 M), 4 $\text{ohm}\cdot\text{cm}^2$ (2 M), and 5.5 $\text{ohm}\cdot\text{cm}^2$ (3 M), respectively (Figure S5f–g, Supporting Information).

2.2. Electrochemical Performance of GPE/bilayer Ta-LLZO Cells

The electrochemical cycling performance of all our garnet Li–S cells was tested at 22 °C using a high sulfur mass loading of 5.2 mg cm^{-2} and different GPE concentrations. The 1 M GPE cell was unable to properly cycle due to an infinitely long charge time (Figure 2a) at a discharge/charge current density of 0.87/0.435 mA cm^{-2} . The analysis of infinite long charge time phenomenon was given in Section 2.4. Conversely, both the 2 and 3 M GPE cells charged and discharged normally as shown in Figure 2b–f, Figures S6 and S7 (Supporting Information). Note that, the asymmetric discharge/charge current density was applied because of the good capability of maintaining high and stable cell cycling performance as demonstrated by previous results.^[37]

EIS measurements show that the 2 and 3 M GPE cells had total ASR values of only 105 $\text{ohm}\cdot\text{cm}^2$ and 124 $\text{ohm}\cdot\text{cm}^2$, respectively (Figure S8, Supporting Information). Figure 2b–d illustrates the long-term cycling performance of the 2 M (cell #1) and 3 M GPE (cell #2) cells discharged at 0.87 mA cm^{-2} at 22 °C. The 2 M GPE cell demonstrated a high initial capacity of 1542 mAh g^{-1} with an average capacity of 1379 mAh g^{-1} over 60 cycles. Similarly, excellent performance was shown by the 3 M GPE cells, with an average capacity of 1316 mAh g^{-1} . Both the stability under cycling and the magnitude of battery capacity (under high sulfur mass loading and high current density) suggest that a stable cathode/electrolyte interface was successfully formed with almost no capacity fade for 60 cycles.

In Figure 2e the cycling stability of both the 2 M (cell #3) and the 3 M (cell #4) GPE remained after increasing the discharge current density to 1.74 mA cm^{-2} . The average discharge capacity of the 2 M GPE cell was 1218 mAh g^{-1} for the first 265 cycles with 80% capacity retention. The average discharge and charge voltage was 1.73 V and 2.26 V, respectively. Note that, the 80% capacity retention was calculated after the capacity of cell #3 was stabilized at the 5th cycle. The 3 M GPE cell had an average discharge capacity of 1116 mAh g^{-1} over 200 cycles. The voltage profile of cell #3 and cell #4 is shown in Figure S6 (Supporting Information).

In Figure 2f, the capacity recoverability of the 2 M GPE design was evaluated using cell #5 for a sequence of discharge current densities: 1.74 mA cm^{-2} (0.2C, 1C = 1670 mA g^{-1}), 2.61 mA cm^{-2} (0.3C), 4.35 mA cm^{-2} (0.5C), 8.7 mA cm^{-2} (1C) and then back to 1.74 mA cm^{-2} (0.2C), with 10 cycles for each condition. It was observed that the average discharge capacity for the 10 cycles at 8.7 mA cm^{-2} was as high as 1015 mAh g^{-1} , 74% of the average discharge capacity (1375 mAh g^{-1}) at 1.74 mA cm^{-2} . When the cell was switched from 8.7 mA cm^{-2} back to 1.74 mA cm^{-2} , the final average discharge capacity was 1293 mAh g^{-1} , which was comparable to the initial average discharge capacity observed for the first 10 cycles at 1.74 mA cm^{-2} . (The voltage profile of the test is shown in Figure S7, Supporting Information.) This demonstrates that even relatively high discharge C-rates for Li–S cells are possible with our GPE-stabilized sulfur cathode/Ta-LLZO interface.

2.3. Cell Performance Comparison

Achieved cycle number, average discharge capacity, and energy density are critical factors for battery performance evaluation. Cell #3 (Figure 2e), which achieved an average discharge capacity of 1218 mAh g^{-1} for over 265 cycles, outperformed previously published garnet Li–S cells, as shown in Figure 3a,b, especially in terms of sulfur loading, average discharge capacity, and energy density.

Similarly, cell #1 produced a high initial discharge capacity of 1542 mAh g^{-1} (Figure 2d) at 0.87 mA cm^{-2} , which corresponds to an energy density of 223 Wh kg^{-1} (769 Wh L^{-1}), shown in Figure 3b–d. This is among the highest values reported for garnet Li–S cells to date. Moreover, by simply reducing the dense layer thickness to our previously demonstrated 10 μm ,^[22] we can project an energy density of 296 Wh kg^{-1} (924 Wh L^{-1}), as indicated in Figure 3c,d. The energy density calculation approach was

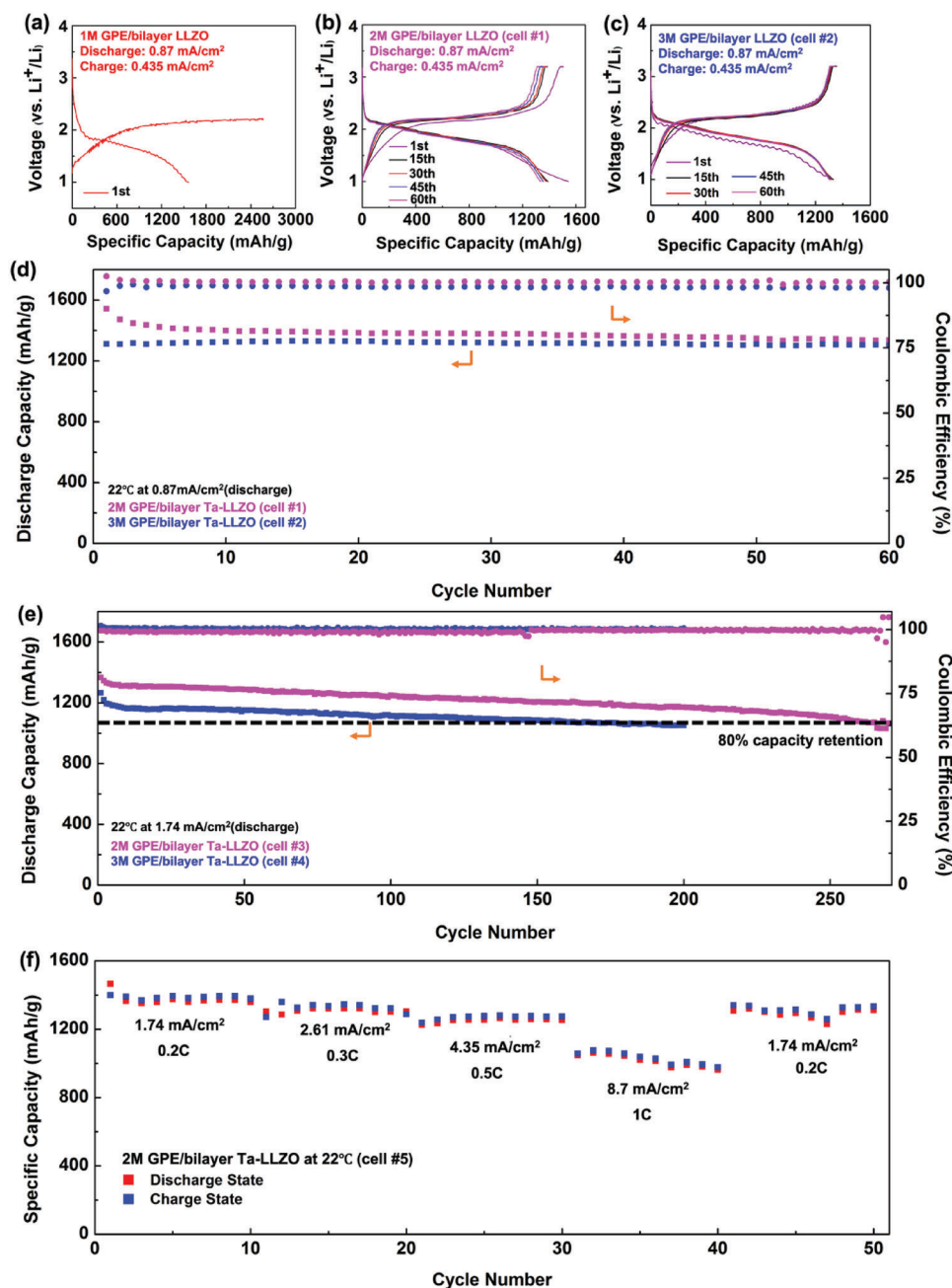


Figure 2. The electrochemical performance tests of our GPE/bilayer Ta-LLZO designs. a) The voltage profile of the 1 m GPE cell. The charge process cannot be finished. b,c) Cycling performances of 2 and 3 m GPE cells, respectively. d) Cycling performances of 2 and 3 m GPE cells. The discharge and charge current density for (a–d) are 0.87 mA cm^{-2} and 0.435 mA cm^{-2} , respectively. e). Cycling performances of 2 and 3 m GPE cells at a discharge current density of 1.74 mA cm^{-2} . f). Capacity recoverability/C-rate performances of the 2 m GPE design ranging from 1.74 mA cm^{-2} to 8.7 mA cm^{-2} and then back to 1.74 mA cm^{-2} . Note that, C-rate is based on the theoretical capacity of elemental sulfur.

the same as our previous results^[24] and can be found in Table S2 (Supporting Information). A comparison of our work with state-of-the-art results for garnet Li–S cells is shown in Table S3 (Supporting Information).

In addition, for a projected Ta-LLZO dense-layer thickness of $10 \mu\text{m}$, further energy density projections based on different sulfur loading (mg cm^{-2}) are shown in Figure S9 (Supporting Information). For example, for a sulfur loading of 7.5 mg cm^{-2} as we

previously demonstrated,^[38] an energy density of 361 Wh kg^{-1} and 1116 Wh L^{-1} is achievable.

2.4. Cell Stability Characterization

X-Ray Diffraction (XRD) scans were used to study the phase stability of the bilayer Ta-LLZO after battery cycling. As shown in

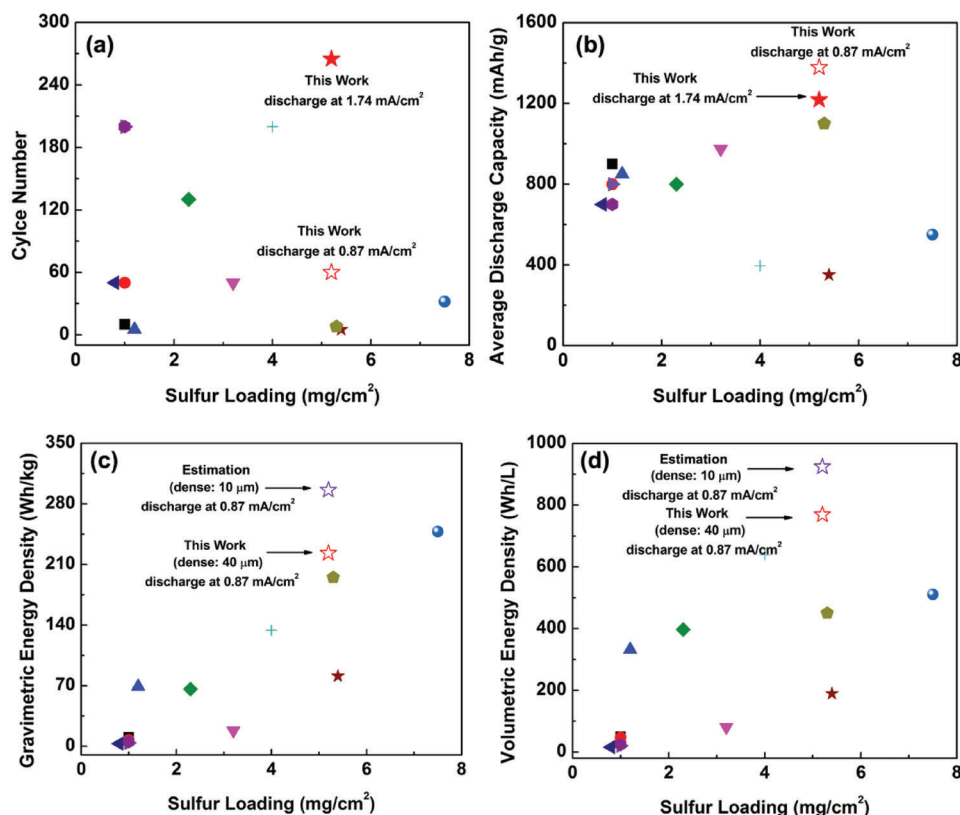


Figure 3. Cell performance evaluation. a, b) and c, d) are the comparison of total number of cycles, average discharge capacity, gravimetric, and volumetric energy densities, respectively. Note that, open red star and open violet star indicated the demonstrated and projected energy densities, respectively. The detailed values are quantified in Table S3 (Supporting Information) with references cited.

Figure S10 (Supporting Information), pure cubic Ta-LLZO was well maintained after cycling the 1, 2, and 3 M GPE cells, indicating there were no crystal structure changes in the Ta-LLZO during the SPAN de-lithiation/lithiation process. These measurements confirmed the phase structure stability of the Ta-LLZO in our GPE/bilayer Ta-LLZO design.

Interfacial decomposition between Ta-LLZO and GPE due to electrochemical reactions were investigated by X-ray photoelectron spectroscopy (XPS). **Figure 4** shows the C 1s and F 1s spectra of Ta-LLZO which confirm the prolonged charging issue in 1 M GPE compared to the cycled charge-discharge in 3 M GPE. The largest difference in the decomposition between 1 M GPE cells and 3 M GPE cells was in the comparative magnitude of the fluorinated carbon peak in the XPS spectra. In the C 1s spectra, the lowest binding energy peak is a hydrocarbon at 284.8 eV,^[39] A peak at 286.2 eV is attributed to C–O bonds,^[40] which is likely from decomposed GPE. A peak at 288.3 eV is attributed to ketones,^[40] and a peak \approx 289.7 eV is attributed to carbonates.^[40] Ketones and carbonates are expected to be decomposition products from GPE. In contrast to the C 1s spectra from 3 M GPE (Figure 4b), a prominent peak of fluorinated carbon^[40] is observed, while the peak of fluorinated carbon in 1 M GPE shown in Figure 4a is very small. The higher amount of fluorinated carbon in 3 M GPE cell compared to the 1 M GPE cell suggests that there was a greater amount of fluorinated decomposition products formed at LLZO surface at higher concentrations.

In the F 1s spectra, a peak \approx 684.8 eV is attributed to LiF.^[39,40] The amount of LiF increased for the 3 M GPE (Figure 4d) to nearly double the amount in 1 M GPE (Figure 4c). A peak \approx 688.3 eV is attributed to decomposed FSI^[24] and a peak \approx 689.4 eV is attributed to fluorinated carbons.^[39,40] The amount of fluorinated carbon in F 1s is significantly higher in 3 M GPE than in 1 M GPE, which is consistent with the results from C 1s spectra. The peak areas of decomposed FSI and fluorinated carbon relative to LiF peak area are larger in 3 M GPE than 1 M GPE. The increase in the ratio of decomposed FSI and fluorinated carbon over LiF indicates that there was difference in decomposition process of FSI. As indicated in both F 1s and C 1s spectra, increased amounts of LiF, fluorinated carbon, and decomposed FSI were observed in 3 M GPE compared to 1 M GPE. The ratio of fluorinated carbon and decomposed FSI with respect to LiF was roughly 10 times higher in 3 M GPE than in 1 M GPE, which is higher than the increase of concentration which is three times more. This suggests that the electrochemical reaction at Ta-LLZO surface is concentration-dependent. This difference in the electrochemical reactions may have contributed to successful charging and good capacity retention of 2 and 3 M GPE cells. 2 and 3 M GPE did not show a prolonged charging issue as 1 M GPE. This suggests that the change of the electrochemical reactions due to higher concentration helped to stabilize the Ta-LLZO surface.

This difference in the electrochemical reactions may be attributed to different salt-to-solvent ratios. The higher the

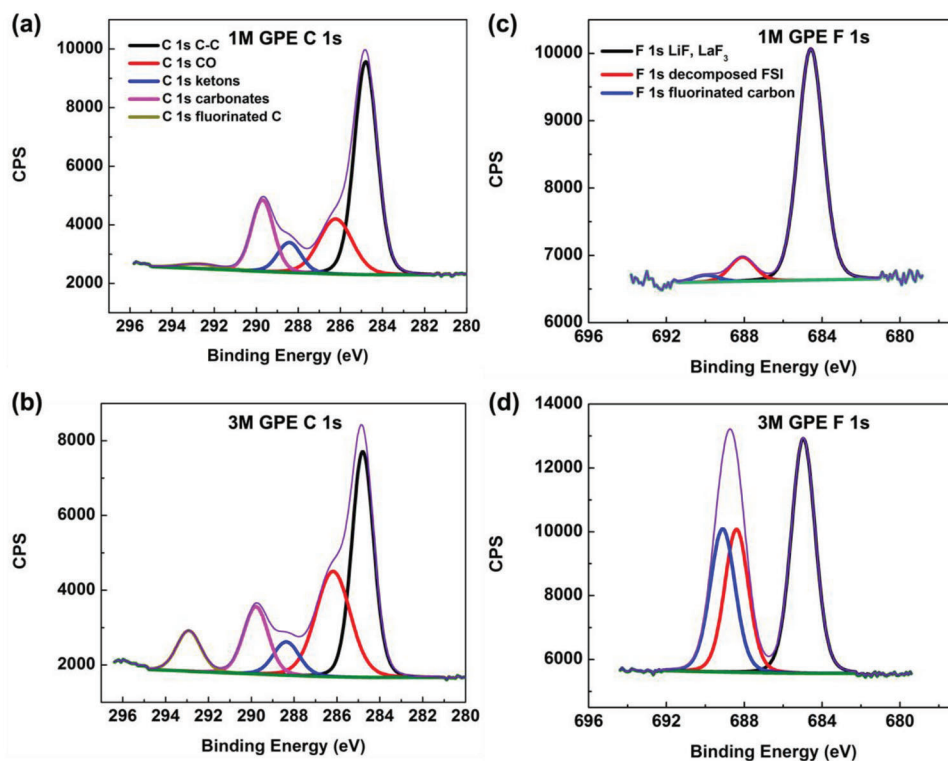


Figure 4. XPS analysis on the electrochemical decomposition between Ta-LLZO and GPE through XPS. C 1s and F 1s spectra of Ta-LLZO charged in 1 M GPE and cycled in 3 M GPE. a,b) show C 1s spectra of 1 M GPE and 3 M GPE, respectively. c,d) shows F 1s spectra of 1 M GPE and 3 M GPE, respectively. The same color was used for the same decomposed compounds in C 1s and F 1s spectra for 1 and 3 M GPE to be easy for comparison.

salt-solvent ratio the greater the decomposition of the salts at the GPE-LLZO interface, which appears to improve its stabilization. Hence, the 1 M GPE cell had an unstable GPE-LLZO interface because of its comparatively lower salt-to-solvent ratio. In a similar organic-salt/organic-solvent system, lithium bis(trifluoromethanesulfonyl)amide (LiTFSa)/acetonitrile (AN) system, it is reported that the decomposition reactions in an electrolyte also change according to its concentration. The authors used DFT-MD simulations to show that the molecule with the unoccupied molecular orbital that is the lowest in the electrolyte (0.4 M LiTFSa/AN) is AN, hence lowest unoccupied molecular orbital (LUMO) is determined by AN. On the other hand, in 4.2 M LiTFSa/AN, TFSa has the unoccupied molecular orbital that is the lowest in the electrolyte, not AN, hence LUMO is determined by TFSa at high concentration. Accordingly, decomposition of AN is preferred in 0.4 M LiTFSa/AN while TFSa anion decomposition is preferred in 4.2 M LiTFSa/AN.^[41,42] The changes of the surface reactions to favor salt decomposition at higher as a function of salt concentration in electrolytes have been reported with various salts (LiFSI, LiTFSa, LiPF₆, LiN(SO₂C₂F₅)₂, LiClO₄, etc), various organic solvents (AN, propylene carbonate (PC), dimethyl sulfoxide (DMSO), DME, ethylene carbonate (EC); diethyl carbonate (DEC), etc) and with various electrode materials (graphite, Li metal, Al, LiNi_{0.5}Mn_{1.5}O₄, LiMn₂O₄, etc).^[41,42,51,43–50] Hence it is reasonable to assume that the decomposition reaction also changed in the LiFSI/poly-DOL + DME system because it was suggested that FSI also becomes the molecule with the unoccupied molecular orbital that is the lowest in the electrolyte as

the concentration of LiFSI increases, which goes along with preferred FSI decomposition over solvents observed by XPS.

Assuming the same analogy of the DFT-MD simulation^[41,42] can be applied, decomposition of FSI was preferred over decompositions of solvents for the 2 and 3 M cell, leading to more LiF, fluorinated carbons and FSI decomposed products formed on Ta-LLZO surface that was characterized by XPS. The Li 1s, S 2p, N 1s, and O 1s spectra of 1 and 3 M GPE are shown in Figures S11 and S12 (Supporting Information), respectively, and discussed in the supporting information. All the XPS spectra of 2 M GPE are shown in Figure S13 (Supporting Information).

In addition to XPS spectra results, the ATR-FTIR spectra (Figure 1b) show that there is –O–C– stretching (1080 cm⁻¹) from DOL in the 1 M GPE cell. This finding suggests the DOL was only partially polymerized in the 1 M GPE. Accordingly, we infer that the incompletely polymerized 1 M GPE still has liquid-like behavior, which allowed the sulfur cathode to come into direct contact with the Ta-LLZO surface and react with a lanthanum-segregated secondary phase,^[24] eventually resulting in cell degradation.

The morphology of the SPAN cathode before and after cycling was characterized through SEM and EDX mapping. As shown in Figure S14a (Supporting Information), the SPAN cathode of the 1 M GPE cell showed severe micro-cracking after discharging at 0.87 mA cm⁻². Conversely, no micro-cracking was visible in the SPAN cathodes of the 2 or 3 M GPE cells (Figure 5a,b). This is because less LiF was formed in the 1 M GPE cells compared with the 2 and 3 M GPE cells (Figure 4). As LiF-rich interfacial layers have been shown to be effective at accommodating

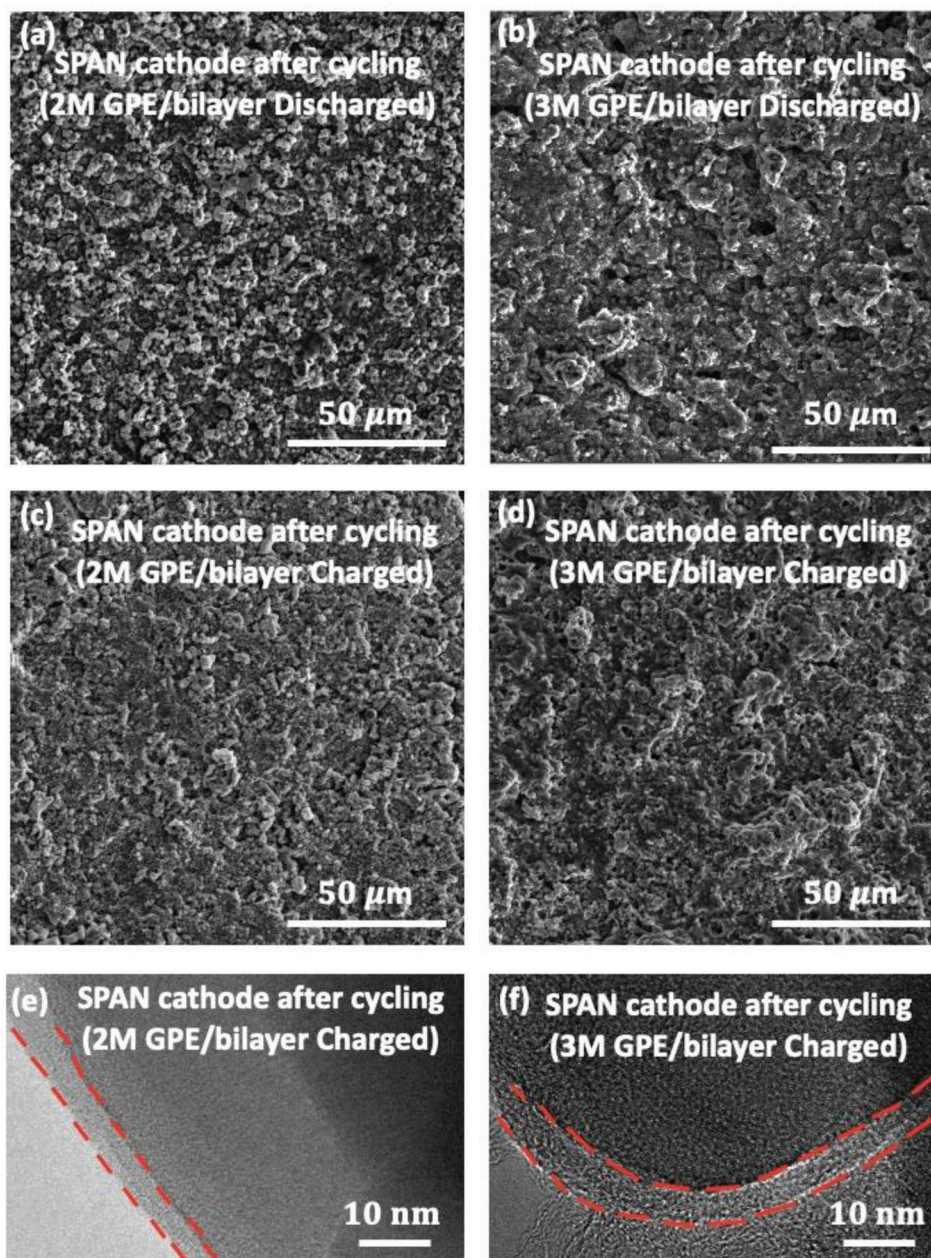


Figure 5. The morphology of SPAN cathode after cycling. a,b). The SPAN cathode under a fully discharged state with an applied discharge current density of 0.87 mA cm^{-2} for 2, and 3 m GPE case, respectively. c,d). The SPAN cathode after cycling under a fully charged state for 2 and 3 m GPE cells, respectively. e,f) are the TEM images of SPAN after cycling in a fully charged state for 2 and 3 m GPE cases, respectively.

the stress/strain evolution resulting from electrode volume change,^[52,53] less LiF formation meant the cathode/LLZO interface was less effective at accommodating the stress/strain, as evidenced by micro-cracking in the SEM images (Figure S14a, Supporting Information). If the 1 m GPE cells could run a complete discharge/charge cycle, we presume it would have had faster capacity decay compared with 2 and 3 m GPE samples due to this microcracking issue. However, in the fully charged state, the SPAN cathodes in both the 2 and 3 m GPE samples (Figure 5c,d) had almost the same morphologies as the pristine SPAN cathode

(Figure S14b, Supporting Information), with no visible micro-cracking or delamination. Maintaining the integrity of the cathode microstructures of the cells was critical to achieving stable cycling performance.^[54] Higher magnification SEM and EDX mapping images and analysis are shown in Figure S15 (Supporting Information).

Transmission electron microscopy (TEM) images in Figure 5e,f revealed a crystalline cathode electrolyte interface (CEI) layer had formed after cycling in the 2 and 3 m GPE cells and were ≈ 4 and 5 nm thick, respectively. A repressive

crystalline nature of CEI is shown in Figure S16 (Supporting Information). The thin and conformal CEI coating layer likely helped passivate the cathode surface, providing a stable cathode/electrolyte interface^[55] and potentially helping to mitigate interfacial stress/strain associated with the sulfur volume expansion which can help produce good particle contact. The elements distribution of CEI cannot be characterized through TEM due to the instability under strong electron beam conditions.

3. Conclusion

By modifying the sulfur cathode/LLZO interface through the addition of an in situ formed GPE interlayer between LLZO for both 2 and 3 M GPE, we fabricated cells that demonstrated stable performance and good energy densities. For the 2 M GPE cells, we obtained a high initial discharge capacity of 1542 mAh g⁻¹ discharged at 0.87 mA cm⁻², corresponding to an energy density of 223 Wh kg⁻¹ and 769 Wh L⁻¹ (cell #1). In addition, the 2 M GPE cell (cell #3) delivered an average discharge capacity of 1218 mAh g⁻¹ (80% capacity retention) over 265 cycles discharged at 1.74 mA cm⁻². This excellent electrochemical performance was principally due to the stabilized SPAN cathode/LLZO interface through the GPE interlayer. In particular, the preferred FSI decomposition over decomposition of the solvents in 2 and 3 M GPE, compared to decomposition of solvents being preferred over FSI decomposition in 1 M GPE. The stabilized sulfur cathode/LLZO interface was likely due to the formation of a completely intimate and conformal CEI coating layer that protected the sulfur cathode/LLZO interface and potentially helped mitigate the stress/strain generated by volume expansion of sulfur cathode. The stability and high performance obtained from this new cell architecture provide a promising pathway for the development of garnet-type solid-state Li-S batteries for practical applications requiring high energy densities.

4. Experimental Section

LLZO Synthesis: Ta-doped LLZO pellets were prepared through a solid-state reaction. Stoichiometric amounts of lithium hydroxide monohydrate (LiOH·H₂O, 98%, Alfa Aesar), tantalum oxide (Ta₂O₅, 99.85%, Alfa Aesar), zirconium oxide (ZrO₂, 99.9%, Inframat Advanced Materials) and preheated lanthanum oxide (La₂O₃, 99.99%, GFS Chemicals) were ball milled and calcined at 900 °C for 10 h in a magnesium oxide crucible. After drying the calcined powder, it was pressed into pellets and covered with sufficient mother powder before sintering at 1100 °C for 8 h. XRD was used to confirm the pellets were pure cubic phase LLZO (Figure S17, Supporting Information). The synthesis process for Ta-doped LLZO bilayer was based on the synthesis process for Nb-doped LLZO discussed in our previous publication,^[20] with the Ta precursor replacing the Nb precursor to form Li_{6.75}La₃Zr_{1.75}Ta_{0.25}O₁₂. Fish oil, toluene, and Isopropyl alcohol were added to the calcinated powder and ball milled for 24 h. Subsequently, benzyl butyl phthalate, polyalkylene glycol, and polyvinyl butyral were weighed out and mixed for another 24 h. After that, the slurry was centrifugally dried for 30–40 min. For the dense layer, the slurry was directly cast at 10 cm min⁻¹ through a doctor blade onto a mylar sheet while being heated at 120 °C. For the porous layer, poly(methyl methacrylate) spheres were added into the slurry and ball milled for another 1 hr before tape casting. The dense tape and porous tape were laminated together using a hot press roller. After that, the bilayer tape was sintered in a tube furnace at 1100 °C. The Li₂CO₃ on the surface of the bilayer LLZO and LLZO pellet was removed by heating the samples to 800 °C for 2 h under inert gas flow.

After that, a ZnO ALD coating layer was deposited using an ATHENA ALD system (Forge Nano Inc.). The thickness of the ZnO ALD coating layer was characterized by Auto ELIII Ellipsometer. ZnO ALD coating characterization data details are shown in Figure S2 (Supporting Information).

Li Metal Anode Fabrication: Pure-Li metal (MTI Corp.) was melted at 265 °C on a hot plate inside an Ar-filled glovebox (O₂ < 0.1 ppm and H₂O < 0.1 ppm). The oxidized molten Li metal surface was carefully removed using a razor blade. The porous layer of the bilayer Ta-LLZO was directly placed onto the molten Li as shown in the video in our previous study^[24] and then the hot plate was cooled to room temperature.

GPE Preparation: Lithium bis(fluorosulfonyl)imide (LiFSI, 99.9%, Alfa Chemistry) was vacuum dried at 120 °C for 24 h before use. DOL (99.8%, Millipore Sigma) and DME (99.5%, Millipore Sigma) solvents were dried by 4 Å molecular sieves (Millipore Sigma) for at least 3 days before use. The liquid solutions of 1 M/2 M/3 M LiFSI in DOL were drop-casted on the dense side of the bilayer LLZO, followed by heating to 45 °C overnight and then resting at 22 °C for 24 h to enable DOL polymerization. After that, a solution of 1 M LiFSI in DME was drop-cast on top of the polymerized DOL, creating the GPE. The solutions of 1 M/2 M/3 M LiFSI in DOL and solution of 1 M LiFSI in DME were mixed in volume ratios of 1:1. All preparations were performed in an Ar-filled glovebox.

SPAN Cathode Preparation: Elemental sulfur (S, Millipore Sigma) and polyacrylonitrile (PAN, M_w ≈ 151 000, Millipore Sigma) were mixed with a mass ratio of 8:1 and a high-energy ball was milled overnight. After that, the S and PAN mixture was heated to 300 °C at a heating rate of 5 °C min⁻¹, held at 300 °C for 7.5 h under flowing Ar, and then cooled to 25 °C. The sulfur was 44 wt% of the SPAN material (Table S4, Supporting Information). The SPAN obtained was amorphous in our previous publication.^[56] The obtained SPAN powder was mixed with carbon black (H.M. Royal Inc.) in a mass ratio of 8:2 under and dispersed in N-Methyl-2-pyrrolidone (NMP, 99.5%, Millipore Sigma), followed by strong stirring to ensure uniform mixing. The SPAN/carbon black suspension was then drop-cast onto a carbon felt to achieve a sulfur mass loading of 5.2 mg cm⁻², followed by drying at 100 °C overnight in an Ar-filled glovebox with O₂ < 0.01 ppm and H₂O < 0.30 ppm.

Electrochemical Measurement: 2032-type coin cells (MTI Corp.) were used for all battery cycling measurements, which were conducted using an Arbin BT 2000 instrument. The coin cells were rested at 22 °C for at least 24 h before cycling. The voltage cutoffs were set to 1 and 3.2 V (vs Li⁺/Li), followed by a constant voltage charge at 3.2 V until the current fell to 0.087 mA cm⁻². A current density of 0.435 mA cm⁻² was used during the constant-current charge process for all the battery tests. The capacity was calculated based on the mass of sulfur in the SPAN. EIS measurements for calculating GPE conductivity were performed by a Solartron 1260 Impedance/Gain-phase Analyzer, and a stainless steel/GPE/stainless steel cell configuration was used. The EIS measurements of GPE conductivity were performed in an Ar-filled glovebox. The conductivity of GPE was calculated using Ohm's law: $\sigma = \frac{1}{R} \frac{L}{A}$, where R, A, and L are the total resistance, the area, and the thickness of the GPE, respectively. The GPE/LLZO interfacial EIS and GPE/sulfur cathode interfacial EIS were measured by using a Bio-logic VSP-300 potentiostat. Impedance curve fitting was performed using the Z-fit software. See the Supporting Information for the equations used.

Characterization: 1). SEM and EDX images were captured with a Tesla GAIA FEG SEM. All samples were washed with NMP and DME solvents and dried before characterization. 2). ATR-FTIR was recorded by NEXUS 670 FTIR instrument. The background signal was subtracted before any ATR-FTIR measurement. 3). The elemental analysis was conducted by LECO 628 carbon nitrogen analyzer to measure the sulfur content concentration in the SPAN. Samples were combusted at 950 °C and CO₂ was measured by infrared detection, while the nitrogen gas was measured for thermal conductivity. Results were reported as percent carbon (%C) and percent nitrogen (%N) and calculated from the mass of the sample placed inside a Tin sample cup (Table S4, Supporting Information). 4). Thermogravimetric Analysis (TGA) was carried out using TGA-50 (Shimadzu Inc) under pure N₂ gas flow with a ramping rate of 1 °C min⁻¹ to 30 °C. To better demonstrate the thermal stability of GPE at elevated temperatures, the program was set to hold at 30 °C for 15 min, followed

by a ramping rate of 3 °C min⁻¹ to 300 °C. 5). TEM observation was performed on JEM 2100F (JEOL, Japan) at 200 keV. All samples were washed with NMP and DME solvents and dried before characterization. 6). XRD was performed using a C2 Discover diffractometer (Bruker AXS) with a Cu K_α radiation source ($\lambda = 1.54056 \text{ \AA}$) operated at 40 kV and 40 mA. The samples were rinsed with NMP and DME solvents before XRD measurements. 7). All the samples were transferred to He glove box in a sealed bag prior to XPS measurements. The glove box atmosphere was kept at < 0.1 ppm O₂ and < 0.0 ppm H₂O. The samples were loaded on a ca. 2 cm diameter puck with Cu tape and transferred to an XPS chamber without air exposure using an air-tight transfer vessel. XPS spectra were obtained with the Kratos Axis Ultra DLD using monochromatic Al K_α (10 mA, 15 kV). XPS scans were carried out at 20 eV pass energy. A charge neutralizer was used during the measurements with a filament current of 1.8 A and a charge balance of 2.5 V. XPS spectra was analyzed with CasaXPS.^[57] All the spectra were referred to C 1s peak of hydrocarbon at 284.8 eV. Tougaard-type background was subtracted before deconvolution and analysis of the peaks.

Supporting Information

Supporting Information is available from the Wiley Online Library or from the author.

Acknowledgements

The authors would like to thank the DEVCOM Army Research Laboratory (ARL) under Cooperative Agreement (CA) Number W911NF-20-2-0284 and Department of Energy, Advanced Research Projects Agency-Energy (ARPA-E) Contract No. DEAR0000787 for their financial support. The authors would like to acknowledge Dr. Yaoyu Ren to give inputs on bilayer Ta-LLZO fabrication, An Phan and Dr. Ai-Min Li from Professor Chunsheng Wang's research group at the University of Maryland (UMD) for providing SPAN powder, X-ray Crystallography Center at UMD for their characterization support, Dr. Jiancun Rao (AIM Lab, Maryland Nanocenter, UMD) for TEM technical support and Dr. Keith Duncan and Griffin Godbey for manuscript discussion. In addition, the authors would also like to thank Nora Hamovit at UMD for conducting the Elemental Analysis on SPAN powder. The authors would also like to thank the National Institute of Standards and Technology for their characterization support. Certain commercial equipment, instruments, materials, suppliers, or software were identified in this paper to foster understanding. Such identification did not imply recommendation or endorsement by the National Institute of Standards and Technology, nor did it imply that the materials or equipment identified are necessarily the best available for the purpose.

Conflict of Interest

Dr. Eric D. Wachsman founded Ion Storage Systems (ION) to commercialize solid-state batteries. However, all results reported herein were performed at the University of Maryland under federal sponsorship.

Author Contributions

The manuscript was written through the contributions of all authors. Specifically, C.S. and E.W. planned the project. E.W. supervised all aspects of the research. C.S. prepared and electrochemically tested the proposed GPE/bilayer cells. C.S. and T.H. performed the SEM/EDX and XRD characterizations. S.T. and J.A.D. conducted XPS experiments and analyzed the results. G.V.A. prepared the Ta-LLZO pellets and helped analyze the results. J.O. draw the schematic fabrication process using Blender software. The manuscript was written by C.S. and E.W. and was revised by the other co-authors.

Data Availability Statement

The data that support the findings of this study are available from the corresponding author upon reasonable request.

Keywords

bilayer LLZO structure, high energy density, high mass loading, in situ formed polymer-based catholytes, Li-S batteries

Received: May 30, 2023

Revised: September 1, 2023

Published online: September 24, 2023

- [1] X. Yang, J. Luo, X. Sun, *Chem. Soc. Rev.* **2020**, *49*, 2140.
- [2] A. Manthiram, X. Yu, S. Wang, *Nat. Rev. Mater.* **2017**, *2*, 16103.
- [3] P. G. Bruce, S. A. Freunberger, L. J. Hardwick, J.-M. Tarascon, *Nat. Mater.* **2012**, *11*, 19.
- [4] S. Zhang, *Energies* **2012**, *5*, 5190.
- [5] C. Wang, K. Fu, S. P. Kammampata, D. W. Mcowen, A. J. Samson, L. Zhang, G. T. Hitz, A. M. Nolan, E. D. Wachsman, Y. Mo, V. Thangadurai, L. Hu, *Chem. Rev.* **2020**, *120*, 4257.
- [6] H. J. Peng, J. Q. Huang, X. B. Cheng, Q. Zhang, *Adv. Energy Mater.* **2017**, *7*, 1.
- [7] N. Kamaya, K. Homma, Y. Yamakawa, M. Hirayama, R. Kanno, M. Yonemura, T. Kamiyama, Y. Kato, S. Hama, K. Kawamoto, A. Mitsui, *Nat. Mater.* **2011**, *10*, 682.
- [8] Z. Zhang, Y. Shao, B. Lotsch, Y.-S. Hu, H. Li, J. Janek, L. F. Nazar, C.-W. Nan, J. Maier, M. Armand, L. Chen, *Energy Environ. Sci.* **2018**, *11*, 1945.
- [9] R. Murugan, V. Thangadurai, W. Weppner, *Angew. Chemie – Int. Ed.* **2007**, *46*, 7778.
- [10] Z. Lin, Z. Liu, W. Fu, N. J. Dudney, C. Liang, *Angew. Chemie – Int. Ed.* **2013**, *52*, 7460.
- [11] D. Rettenwander, A. Welzl, L. Cheng, J. Fleig, M. Musso, E. Suard, M. M. Doeff, G. J. Redhammer, G. Amthauer, *Inorg. Chem.* **2015**, *54*, 10440.
- [12] X. Liu, R. Garcia-Mendez, A. R. Lupini, Y. Cheng, Z. D. Hood, F. Han, A. Sharafi, J. C. Idrobo, N. J. Dudney, C. Wang, C. Ma, J. Sakamoto, M. Chi, *Nat. Mater.* **2021**, *20*, 1485.
- [13] F. Han, J. Yue, C. Chen, N. Zhao, X. Fan, Z. Ma, T. Gao, F. Wang, X. Guo, C. Wang, *Joule* **2018**, *2*, 497.
- [14] X. Han, Y. Gong, K. Fu, X. He, G. T. Hitz, J. Dai, A. Pearse, B. Liu, H. Wang, G. Rubloff, Y. Mo, V. Thangadurai, E. D. Wachsman, L. Hu, *Nat. Mater.* **2017**, *16*, 572.
- [15] V. Thangadurai, S. Narayanan, D. Pinzaru, *Chem. Soc. Rev.* **2014**, *43*, 4714.
- [16] F. Han, A. S. Westover, J. Yue, X. Fan, F. Wang, M. Chi, D. N. Leonard, N. J. Dudney, H. Wang, C. Wang, *Nat. Energy* **2019**, *4*, 187.
- [17] Z. Bi, Q. Sun, M. Jia, M. Zuo, N. Zhao, X. Guo, *Adv. Funct. Mater.* **2022**, *32*, 2208751.
- [18] Z. Bi, W. Huang, S. Mu, W. Sun, N. Zhao, X. Guo, *Nano Energy* **2021**, *90*, 106498.
- [19] G. T. Hitz, D. W. Mcowen, L. Zhang, Z. Ma, Z. Fu, Y. Wen, Y. Gong, J. Dai, T. R. Hamann, L. Hu, E. D. Wachsman, *Mater. Today* **2019**, *22*, 50.
- [20] K. (K.). Fu, Y. Gong, G. T. Hitz, D. W. Mcowen, Y. Li, S. Xu, Y. Wen, L. Zhang, C. Wang, G. Pastel, J. Dai, B. Liu, H. Xie, Y. Yao, E. D. Wachsman, L. Hu, *Energy Environ. Sci.* **2017**, *10*, 1568.
- [21] B. Liu, L. Zhang, S. Xu, D. W. Mcowen, Y. Gong, C. Yang, G. R. Pastel, H. Xie, K. Fu, J. Dai, C. Chen, E. D. Wachsman, L. Hu, *Energy Storage Mater.* **2018**, *14*, 376.

- [22] S. Xu, D. W. Mcowen, L. Zhang, G. T. Hitz, C. Wang, Z. Ma, C. Chen, W. Luo, J. Dai, Y. Kuang, E. M. Hitz, K. Fu, Y. Gong, E. D. Wachsman, L. Hu, *Energy Storage Mater.* **2018**, *15*, 458.
- [23] Z. Fu, E. D. Wachsman, *J. Am. Ceram. Soc.* **2023**, *6*, 1.
- [24] C. Shi, T. Hamann, S. Takeuchi, G. V. Alexander, A. M. Nolan, M. Limpert, Z. Fu, J. O'neill, G. Godbey, J. A. Dura, E. D. Wachsman, *ACS Appl. Mater. Interfaces* **2023**, *15*, 751.
- [25] M. Shaibani, M. S. Mirshekarloo, R. Singh, C. D. Easton, M. C. D. Cooray, N. Eshraghi, T. Abendroth, S. Dörfler, H. Althues, S. Kaskel, A. F. Hollenkamp, M. R. Hill, M. Majumder, *Sci. Adv.* **2020**, *6*, aay2757.
- [26] S.-H. Chung, A. Manthiram, *Adv. Mater.* **2019**, *31*, 1901125.
- [27] J. Lin, L. Wu, Z. Huang, X. Xu, J. Liu, *J. Energy Chem.* **2020**, *40*, 132.
- [28] M. Naguib, A. Sharafi, E. C. Self, H. M. Meyer, J. Sakamoto, J. Nanda, *ACS Appl. Mater. Interfaces* **2019**, *11*, 42042.
- [29] C.-H. Yu, C.-S. Cho, C.-C. Li, *ACS Appl. Mater. Interfaces* **2021**, *13*, 11995.
- [30] X. Huang, C. Liu, Y. Lu, T. Xiu, J. Jin, M. E. Badding, Z. Wen, *J. Power Sources* **2018**, *382*, 190.
- [31] S. Wei, L. Ma, K. E. Hendrickson, Z. Tu, L. A. Archer, *J. Am. Chem. Soc.* **2015**, *137*, 12143.
- [32] M. S. Ahmed, S. Lee, M. Agostini, M. G. Jeong, H. G. Jung, J. Ming, Y. K. Sun, J. Kim, J. Y. Hwang, *Adv. Sci.* **2021**, *8*, 2101123.
- [33] S. Perez Beltran, P. B. Balbuena, *J. Phys. Chem. C* **2021**, *125*, 13185.
- [34] C. Wang, Y. Gong, B. Liu, K. Fu, Y. Yao, E. Hitz, Y. Li, J. Dai, S. Xu, W. Luo, E. D. Wachsman, L. Hu, *Nano Lett.* **2017**, *17*, 565.
- [35] S. Choi, S. Mugohera, J. M. Ko, K. S. Lee, *Colloids Surf. A Physicochem. Eng. Asp.* **2021**, *631*, 127722.
- [36] C.-W. Chang, H.-H. Hsu, C.-S. Hsu, J.-T. Chen, *J. Mater. Chem. C* **2021**, *9*, 14589.
- [37] T. Jin, Y. Ma, Z. Xiong, X. Fan, Y. Luo, Z. Hui, X. Chen, Y. Yang, *Adv. Energy Mater.* **2021**, *11*, 2100997.
- [38] Z. Yu, H. Wang, X. Kong, W. Huang, Y. Tsao, D. G. Mackanic, K. Wang, X. Wang, W. Huang, S. Choudhury, Y. Zheng, C. V. Amanchukwu, S. T. Hung, Y. Ma, E. G. Lomeli, J. Qin, Y. Cui, Z. Bao, *Nat. Energy* **2020**, *5*, 526.
- [39] A. V. Naumkin, A. Kraut-Vass, S. W. Gaarenstroom, C. J. Powell, "NIST X-ray Photoelectron Spectroscopy Database20, Version 4.1", <http://dx.doi.org/10.18434/T4T88K>, (accessed: September 2012).
- [40] J. Moulder, W. Stickle, P. Sobol, K. Bomben, in *Handbook of X-Ray Photoelectron Spectroscopy (XPS)*, **2005**.
- [41] Y. Yamada, K. Furukawa, K. Sodeyama, K. Kikuchi, M. Yaegashi, Y. Tateyama, A. Yamada, *J. Am. Chem. Soc.* **2014**, *136*, 5039.
- [42] K. Sodeyama, Y. Yamada, K. Aikawa, A. Yamada, Y. Tateyama, *J. Phys. Chem. C* **2014**, *118*, 14091.
- [43] K. Matsumoto, K. Inoue, K. Nakahara, R. Yuge, T. Noguchi, K. Utsugi, *J. Power Sources* **2013**, *231*, 234.
- [44] S.-K. Jeong, M. Inaba, Y. Iriyama, T. Abe, Z. Ogumi, *Electrochem. Solid-State Lett.* **2003**, *6*, A13.
- [45] S.-K. Jeong, M. Inaba, Y. Iriyama, T. Abe, Z. Ogumi, *J. Power Sources* **2008**, *175*, 540.
- [46] Y. Yamada, Y. Takazawa, K. Miyazaki, T. Abe, *J. Phys. Chem. C* **2010**, *114*, 11680.
- [47] Y. Yamada, M. Yaegashi, T. Abe, A. Yamada, *Chem. Commun.* **2013**, *49*, 11194.
- [48] T. Doi, R. Masuhara, M. Hashinokuchi, Y. Shimizu, M. Inaba, *Electrochim. Acta* **2016**, *209*, 219.
- [49] K. Yoshida, M. Nakamura, Y. Kazue, N. Tachikawa, S. Tsuzuki, S. Seki, K. Dokko, M. Watanabe, *J. Am. Chem. Soc.* **2011**, *133*, 13121.
- [50] S. Takeuchi, R. Kokumai, S. Nagata, T. Fukutsuka, K. Miyazaki, T. Abe, *J. Electrochem. Soc.* **2016**, *163*, A1693.
- [51] D. W. Mcowen, D. M. Seo, O. Borodin, J. Vatamanu, P. D. Boyle, W. A. Henderson, *Energy Environ. Sci.* **2014**, *7*, 416.
- [52] J. Chen, X. Fan, Q. Li, H. Yang, M. R. Khoshi, Y. Xu, S. Hwang, L. Chen, X. Ji, C. Yang, H. He, C. Wang, E. Garfunkel, D. Su, O. Borodin, C. Wang, *Nat. Energy* **2020**, *5*, 386.
- [53] X. Fan, X. Ji, F. Han, J. Yue, J. Chen, L. Chen, T. Deng, J. Jiang, C. Wang, *Sci. Adv.* **2018**, *4*, eaau9245.
- [54] W. Xue, M. Huang, Y. Li, Y. G. Zhu, R. Gao, X. Xiao, W. Zhang, S. Li, G. Xu, Y. Yu, P. Li, J. Lopez, D. Yu, Y. Dong, W. Fan, Z. Shi, R. Xiong, C.-J. Sun, I. Hwang, W.-K. Lee, Y. Shao-Horn, J. A. Johnson, J. Li, *Nat. Energy* **2021**, *6*, 495.
- [55] Z. Zhang, J. Yang, W. Huang, H. Wang, W. Zhou, Y. Li, Y. Li, J. Xu, W. Huang, W. Chiu, Y. Cui, *Matter* **2021**, *4*, 302.
- [56] C. Shi, G. V. Alexander, J. O'neill, K. Duncan, G. Godbey, E. D. Wachsman, *ACS Energy Lett.* **2023**, *8*, 1803.
- [57] N. Fairley, V. Fernandez, M. Richard-Plouet, C. Guillot-Deudon, J. Walton, E. Smith, D. Flahaut, M. Greiner, M. Biesinger, S. Tougaard, D. Morgan, J. Baltrusaitis, *Appl. Surf. Sci. Adv.* **2021**, *5*, 100112.